



Modular Paradigm for Scalable Quantum Information

**Paola Cappellaro
MASSACHUSETTS INSTITUTE OF TECHNOLOGY**

**03/04/2016
Final Report**

DISTRIBUTION A: Distribution approved for public release.

**Air Force Research Laboratory
AF Office Of Scientific Research (AFOSR)/ RTB1
Arlington, Virginia 22203
Air Force Materiel Command**

REPORT DOCUMENTATION PAGE

*Form Approved
OMB No. 0704-0188*

The public reporting burden for this collection of information is estimated to average 1 hour per response, including the time for reviewing instructions, searching existing data sources, gathering and maintaining the data needed, and completing and reviewing the collection of information. Send comments regarding this burden estimate or any other aspect of this collection of information, including suggestions for reducing the burden, to the Department of Defense, Executive Service Directorate (0704-0188). Respondents should be aware that notwithstanding any other provision of law, no person shall be subject to any penalty for failing to comply with a collection of information if it does not display a currently valid OMB control number.

PLEASE DO NOT RETURN YOUR FORM TO THE ABOVE ORGANIZATION.

1. REPORT DATE (DD-MM-YYYY) 29-02-2016	2. REPORT TYPE Final Report	3. DATES COVERED (From - To) 01/06/2012-30/11/2015
--	---------------------------------------	--

4. TITLE AND SUBTITLE Young Investigator Program: Modular Paradigm for Scalable Quantum Information	5a. CONTRACT NUMBER FA9550-12-1-0292
	5b. GRANT NUMBER FA9550-12-1-0292
	5c. PROGRAM ELEMENT NUMBER

6. AUTHOR(S) Cappellaro, Paola	5d. PROJECT NUMBER
	5e. TASK NUMBER
	5f. WORK UNIT NUMBER

7. PERFORMING ORGANIZATION NAME(S) AND ADDRESS(ES) MASSACHUSETTS INSTITUTE OF TECHNOLOGY 77 MASSACHUSETTS AVE CAMBRIDGE MA 02139-4301 (617) 324-9022	8. PERFORMING ORGANIZATION REPORT NUMBER
---	---

9. SPONSORING/MONITORING AGENCY NAME(S) AND ADDRESS(ES) Air Force Aerospace Research-OSR 875 N. Randolph Street Arlington, VA 22203 tatjana.curcic@afosr.af.mil 703-696-6204	10. SPONSOR/MONITOR'S ACRONYM(S) AFOSR
	11. SPONSOR/MONITOR'S REPORT NUMBER(S)

12. DISTRIBUTION/AVAILABILITY STATEMENT
Distribution A - Approved for public release

13. SUPPLEMENTARY NOTES

14. ABSTRACT
The goal of the project "Modular Paradigm for Scalable Quantum Information" was to address some of the challenges facing the field of quantum information science (QIS). The requirements to reliably control a scalable quantum system while staving off decoherence pose a contradiction, as fast control implies a strong coupling to a controlling (external) system, but this entails an undesired interaction with the environment, leading to decoherence. We thus studied a new paradigm for QIS, given by smaller building blocks (composed of a quantum register and a controller) that are connected by spin wires. Among the project accomplishments are novel strategies for time-optimal control via a quantum controller, a quantum feedback scheme where the controller is fully quantum, and the first implementation of quantum information transport in a mixed-state spin chain.

15. SUBJECT TERMS
Quantum control; quantum information; quantum spins

16. SECURITY CLASSIFICATION OF:			17. LIMITATION OF ABSTRACT SAR	18. NUMBER OF PAGES	19a. NAME OF RESPONSIBLE PERSON Paola Cappellaro
a. REPORT	b. ABSTRACT	c. THIS PAGE			19b. TELEPHONE NUMBER (Include area code) 617-253-8137

INSTRUCTIONS FOR COMPLETING SF 298

1. REPORT DATE. Full publication date, including day, month, if available. Must cite at least the year and be Year 2000 compliant, e.g. 30-06-1998; xx-06-1998; xx-xx-1998.

2. REPORT TYPE. State the type of report, such as final, technical, interim, memorandum, master's thesis, progress, quarterly, research, special, group study, etc.

3. DATES COVERED. Indicate the time during which the work was performed and the report was written, e.g., Jun 1997 - Jun 1998; 1-10 Jun 1996; May - Nov 1998; Nov 1998.

4. TITLE. Enter title and subtitle with volume number and part number, if applicable. On classified documents, enter the title classification in parentheses.

5a. CONTRACT NUMBER. Enter all contract numbers as they appear in the report, e.g. F33615-86-C-5169.

5b. GRANT NUMBER. Enter all grant numbers as they appear in the report, e.g. AFOSR-82-1234.

5c. PROGRAM ELEMENT NUMBER. Enter all program element numbers as they appear in the report, e.g. 61101A.

5d. PROJECT NUMBER. Enter all project numbers as they appear in the report, e.g. 1F665702D1257; ILIR.

5e. TASK NUMBER. Enter all task numbers as they appear in the report, e.g. 05; RF0330201; T4112.

5f. WORK UNIT NUMBER. Enter all work unit numbers as they appear in the report, e.g. 001; AFAPL30480105.

6. AUTHOR(S). Enter name(s) of person(s) responsible for writing the report, performing the research, or credited with the content of the report. The form of entry is the last name, first name, middle initial, and additional qualifiers separated by commas, e.g. Smith, Richard, J, Jr.

7. PERFORMING ORGANIZATION NAME(S) AND ADDRESS(ES). Self-explanatory.

8. PERFORMING ORGANIZATION REPORT NUMBER. Enter all unique alphanumeric report numbers assigned by the performing organization, e.g. BRL-1234; AFWL-TR-85-4017-Vol-21-PT-2.

9. SPONSORING/MONITORING AGENCY NAME(S) AND ADDRESS(ES). Enter the name and address of the organization(s) financially responsible for and monitoring the work.

10. SPONSOR/MONITOR'S ACRONYM(S). Enter, if available, e.g. BRL, ARDEC, NADC.

11. SPONSOR/MONITOR'S REPORT NUMBER(S). Enter report number as assigned by the sponsoring/monitoring agency, if available, e.g. BRL-TR-829; -215.

12. DISTRIBUTION/AVAILABILITY STATEMENT. Use agency-mandated availability statements to indicate the public availability or distribution limitations of the report. If additional limitations/ restrictions or special markings are indicated, follow agency authorization procedures, e.g. RD/FRD, PROPIN, ITAR, etc. Include copyright information.

13. SUPPLEMENTARY NOTES. Enter information not included elsewhere such as: prepared in cooperation with; translation of; report supersedes; old edition number, etc.

14. ABSTRACT. A brief (approximately 200 words) factual summary of the most significant information.

15. SUBJECT TERMS. Key words or phrases identifying major concepts in the report.

16. SECURITY CLASSIFICATION. Enter security classification in accordance with security classification regulations, e.g. U, C, S, etc. If this form contains classified information, stamp classification level on the top and bottom of this page.

17. LIMITATION OF ABSTRACT. This block must be completed to assign a distribution limitation to the abstract. Enter UU (Unclassified Unlimited) or SAR (Same as Report). An entry in this block is necessary if the abstract is to be limited.

Modular Paradigm for Scalable Quantum Information

Final Report (FA9550-12-1-0292) — June 2012-November 2015

Paola Cappellaro

Massachusetts Institute of Technology Cambridge, MA 02139, USA

1 Objectives and results of the research

The goal of the project “Modular Paradigm for Scalable Quantum Information” was to address some of the challenges facing the field of quantum information science (QIS). The requirements to reliably control a scalable quantum system while staving off decoherence pose a contradiction, as fast control implies a strong coupling to a controlling (external) system, but this entails an undesired interaction with the environment, leading to decoherence. We thus studied a novel paradigm for QIS, given by smaller building blocks (composed of a quantum **register** and an **actuator**) that are connected by **spin wires**.

We obtained significant results in both these tasks. Over the course of the project we developed novel control techniques, such as Hamiltonian engineering for many-body systems [1], and hybrid control combining classical controllers with quantum actuators [2, 3]. A significant result is the first implementation of a feedback control algorithm with an electronic spin qubit in diamond [4]. We experimentally demonstrated protection against naturally occurring dephasing noise, extending the electronic spin qubit coherence time by three orders of magnitude. This is a critical step toward building fault-tolerant quantum devices and it will also contribute to the wider application of quantum feedback. In addition, we explored means to connect distributed registers via *spin wires*, by performing the first demonstration of quantum information transport with a mixed-state spin wire [5]. We further explored the effects of noise and disorder on quantum information transport, elucidating some complex dynamics [6] and the emergence of localization.

2 Control and coherence of the quantum actuator/register system

The first activity of the project was to develop control strategies for the actuator/register system and to implement them experimentally.

While semiclassical techniques are adequate for simple manipulation of spins, such as traditional NMR studies of bulk systems, the key challenge for modern quantum engineering is to achieve near-perfect control fidelity in the presence of strong coupling to the environment. To meet this challenge, we moved beyond the control paradigms used in the past, devising control techniques beyond the usual rotating wave approximation [7] and combining coherent control and dissipation for state preparation [8].

An innovative theme of this research program has been to exploit quantum systems themselves as controllers. Using a quantum actuator can allow faster control; it avoids additional noise sources linked to a classical apparatus; and it can achieve a higher degree of spatial resolution.

We thus studied time-optimal control via a quantum actuator [2] and investigated when this strategy can beat driving by a classical field [9]. Significantly, we demonstrated experimentally that combining quantum and classical controllers can achieve even faster control [3]. A quantum controller is often also the best option to implement feedback control, a particularly efficient strategy to protect qubits from detrimental noise while implementing desired operations. Open-loop control such as dynamical decoupling suppresses slowly varying phase noise and enhances the qubit coherence time. However, it is ineffective against fast-varying noise and often lacks compatibility with quantum gates. Feedback-based control could overcome these difficulties and is indeed the method of choice for the control of classical systems. Nonetheless, as feedback usually entails destructive measurements that complicate the qubit dynamics, until our work the implementation of feedback protocols had been limited mainly to quantum optics. Using the NV nitrogen

nuclear spin as an ancillary qubit, we experimentally demonstrated protection against naturally occurring dephasing noise, extending the electronic spin qubit coherence time by three orders of magnitude [4]. This feedback scheme is compatible with applications of gates on the protected qubit, as we demonstrated by performing a protected NOT gate. I expect that this demonstration of the power of feedback control for the precise manipulation of quantum systems will contribute to its widespread application, analogous to its success in classical control.

Among our results,

- We found the shape of the time-optimal control strategy to engineer desired qubit gates via the actuator control. Using algebraic methods we were able to find the time-optimal control solutions for the most general SU(2) synthesis problem.
- We derived new bounds on the time and number of switches required to engineer desired qubit gates via the actuator control that are more general and stricter than previously known bounds.
- We developed an efficient numerical method to find the time-optimal control sequence and applied it to find gates for the coupled NV-nuclear spin system.
- We devised a method to implement time-optimal bang-bang control in the practical situations where the experimental control doesn't have infinite bandwidth and quantified the ensuing loss of fidelity.
- We characterized experimentally the nitrogen nuclear spin Hamiltonian, devising a method to measure the full hyperfine tensor. This measurement had not been possible until now for single NV centers.
- We exploited the control achieved on the nitrogen nuclear spin to implement a feedback algorithm to preserve the coherence of the NV electronic spin

Details of these activities are described below.

2.1 Optimal control of a qubit by a quantum actuator

A central goal of the project was to devise and demonstrate quantum control techniques where the controlling apparatus itself is a quantum system. Using a quantum controller can allow faster dynamics; it avoids additional noise sources linked to a classical apparatus; and it can achieve a higher degree of spatial resolution. We focused our attention to the control of well-isolated single spin qubits by a quantum controller (itself a spin qubit), which is strongly coupled to external driving fields. The goal is the generation of desired unitaries (or gates) to control the system for any initial state. The Hamiltonian of the system can be written as

$$\tilde{\mathcal{H}}_0 = \omega_L \sigma_z + S_z^a \vec{A} \cdot \vec{\sigma}, \quad (1)$$

where S_z^a refers to the actuator spin and $\vec{\sigma}$ to the nuclear spin in the register. A simple control strategy is to let the actuator alternate between two possible states by applying π -pulses at designated times t_k . Then the Hamiltonian (1) alternates between two non-commuting operators $\hat{z} = \omega_L \sigma_z$ and $\hat{v} = \omega_L \sigma_z + \vec{A} \cdot \vec{\sigma}$. Switching between the actuator eigenstates is enough to achieve full controllability of the qubit, as long as the coupling is anisotropic [10, 11]. In the absence of direct driving of the qubit, Pontryagin's minimum principle proves that this bang-bang control achieves time-optimality [12–14] and one needs to find a series of switching times $\{t_k\}$ that give the desired evolution.

More generally, we aim at solving the problem of generating a transformation in SU(2) [or SO(3)] when the available control is given by rotations around two non-parallel axes, \hat{x} and $v = \kappa(\cos \alpha \hat{x} + \sin \alpha \hat{y})$, with $\kappa \geq 1$, with clockwise ($t_k > 0$) rotations only or both clockwise and anti-clockwise rotations ($t_k \gtrless 0$). Thus, any allowed control sequence can be written as

$$U = X(t_1) V(t_2) \dots, X(t_{x,k}) V(t_{v,k+1}) \dots, \quad \text{with } X(t) = e^{-i\hat{\sigma} \cdot \hat{x} t/2}, \quad V(t) = e^{-i\hat{\sigma} \cdot \vec{v} t/2} \quad (2)$$

We used an algebraic framework to study this time-optimal synthesis problem, which is common in both quantum and classical mechanics. The method we used bypasses usual control-theoretical techniques, and

easily imposes necessary conditions on time-optimal sequences. We thus derive the fact that time-optimal sequences are solely parametrized by three rotation angles and a finite combination of signs [2].

Case $t > 0$. Time-optimal sequences only depend on four parameters, namely the total number of rotations $n \leq \infty$, the outer angles t_1, t_n and the internal angle t_x (or t_v). In this case, the internal angles are related by

$$\tan\left(\frac{t_v}{2}\right) = \tan\left(\frac{t_x}{2}\right) \frac{\kappa - \cos(\alpha)}{1 - \kappa \cos(\alpha)}. \quad (14)$$

Case $t \leq 0$. It holds that either $n \leq 5$, or $n \rightarrow \infty$. Time-optimal sequences only depend on four parameters, as above, and a few combinations of signs (only four signs need to be specified). Internal angles are related by

$$\tan\left(\frac{t_v}{2}\right) = \pm \tan\left(\frac{t_x}{2}\right) \frac{1}{\kappa} \quad (18)$$

in finite sequences; and, in infinite sequences

$$\tan\left(\frac{t_v}{2}\right) = \tan\left(\frac{t_x}{2}\right) \frac{\kappa - \cos(\alpha)}{1 - \kappa \cos(\alpha)}; \quad (22)$$

$$\tan\left(\frac{t_v}{2}\right) = -\tan\left(\frac{t_x}{2}\right) \frac{\kappa + \cos(\alpha)}{1 + \kappa \cos(\alpha)}. \quad (23)$$

Furthermore, we were able to derive general bounds on the times as a function of the angle between the axes and the relative rotation speed of each control. Results are substantially different whether both clockwise and counterclockwise rotations about the given axes are allowed, or only clockwise rotations. In the first case, we proved that any finite time-optimal sequence is composed at most of five control concatenations, while for the more restrictive case, we found scaling laws on the maximum length of any finite time-optimal sequence; bounds for both cases are stricter than previously published ones. These bounds severely constrain the structure of time-optimal sequences, allowing for a simple numerical search of the time-optimal solution. We note that besides the application to our present quantum control, the theory is much more general and can be applied even to classical rotations, for example for robotics applications.

Our theoretical results can be immediately used to the problem of controlling nuclear spins coupled to the NV center in diamond. As a concrete example, we consider a single NV center electronic spin $S = 1$ coupled to a ^{13}C nuclear spin $I = 1/2$. Their Hamiltonian is

$$\mathcal{H} = \Delta S_z^2 + \gamma_e B_0 S_z + \gamma_C B_0 I_z + \vec{S} \cdot \mathbf{A} \cdot \vec{I}, \quad (3)$$

where $\Delta = 2.87\text{GHz}$ is the NV zero-field splitting; $\gamma_e \approx 2.8\text{MHz/G}$, $\gamma_C \approx 1\text{kHz/G}$ are, respectively, the gyromagnetic ratios of the electron and nuclear spins; B_0 is a static magnetic field along the NV \hat{z} -axis; and \mathbf{A} is the hyperfine tensor. The NV spin triplet can be reduced to an effective two-level system by driving the system on resonance with a transition between two S_z eigenstates (e.g. $|m_s = 0\rangle \leftrightarrow |m_s = +1\rangle$), while the third eigenstate (e.g. $|m_s = -1\rangle$) can be neglected. Then the Hamiltonian can be rewritten in the electronic spin rotating frame as

$$\mathcal{H} = \omega_0 I_z + S_z \vec{A}_z \cdot \vec{I} = |0\rangle\langle 0| \omega_0 I_z + |\pm 1\rangle\langle \pm 1| (\omega_0 I_z \pm \vec{A}_z \cdot \vec{I}), \quad (4)$$

where $\omega_0 = \gamma_C B_0$ (that we assume > 0). The contact and dipolar contributions [15] to the hyperfine coupling \vec{A} can be described by a longitudinal component A_{\parallel} and a transverse component A_{\perp} , that we will take without loss of generality along the \hat{x} direction. The nuclear spin thus rotates around two distinct axes, depending on the electronic spin manifold. Then, a simple strategy for the indirect control of the nuclear spin is to induce alternating rotations by flipping the electronic spin state with (fast) π -pulses. We define the axes and rotation speeds in the two manifolds as

$$\begin{aligned} \omega_0 &= \gamma_C B_0 = \kappa \omega_{\pm 1}, & \omega_{\pm 1} &= \sqrt{(\omega_0 \pm A_{\parallel})^2 + A_{\perp}^2}, \\ \hat{v}_0 &= \hat{z}, & \hat{v}_{\pm 1} &= \hat{z} \cos(\alpha) + \hat{x} \sin(\alpha), \end{aligned} \quad (5)$$

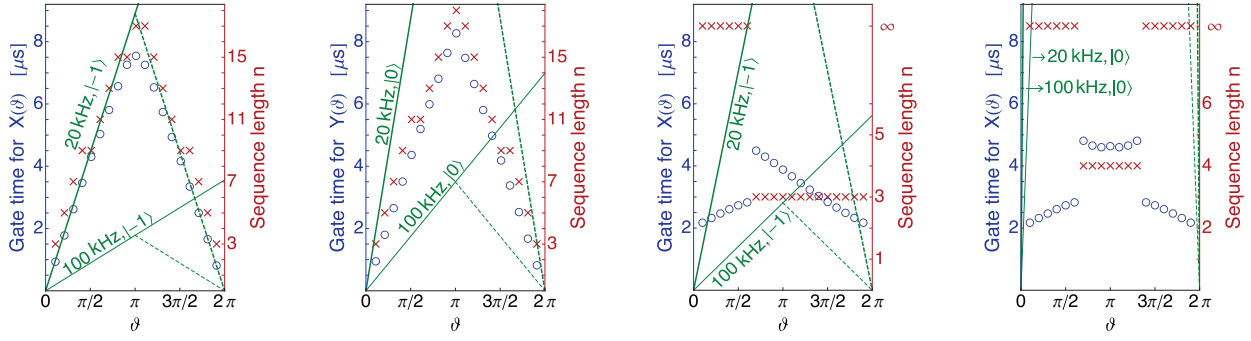


Fig. 1: Comparison of gate time, Left: Case $\kappa < \cos(\alpha)$, occurring for a ^{13}C at a distance of $\approx 2.92\text{\AA}$ from the NV center, with an external magnetic field $B_0 \approx 500\text{G}$ aligned with the \hat{z} axis. We plot the simulated actuator implementation time (blue circles-left axis) of the unitaries $X(\vartheta)$ (left) and $Y(\vartheta)$ (right) and the corresponding sequence lengths (red crosses-right axis). For comparison, we plot the time required with direct driving (green lines) with bare Rabi frequencies 20 and 100kHz, when the electronic spin in state $|-1\rangle$ (left), thus maximizing the enhancement factor, or $|0\rangle$ (right). Note that the direct-driving time for $\vartheta > \pi$ depends on whether the driving phase can be inverted (dashed line) or not (solid line). **Comparison of gate time, Right: Case $\kappa > \cos(\alpha)$** , occurring for a ^{13}C at a distance of $\approx 4.31\text{\AA}$ from the NV center. Note that virtual transition of the electronic spin in the $m_s = 0$ manifold result in a decrease of the effective Rabi frequency, thus making direct driving in that manifold unfavorable.

with
$$\tan(\alpha) = \frac{A_{\perp}}{\omega_0 \pm A_{\parallel}}, \quad \kappa = \frac{\omega_0}{\omega_{\pm 1}}. \quad (6)$$

If the NV electronic spin is initially in the $|0\rangle$ state, applying π -pulses at times T_k gives the nuclear spin evolution:

$$U = e^{-i\varphi_n^1 \vec{v}_1 \cdot \vec{\sigma}} \dots e^{-i\varphi_k^0 \vec{v}_0 \cdot \vec{\sigma}} e^{-i\varphi_{k-1}^1 \vec{v}_1 \cdot \vec{\sigma}} \dots e^{-i\varphi_i^0 \vec{v}_0 \cdot \vec{\sigma}}, \quad (7)$$

where $\varphi_k^{0(1)} = (T_k - T_{k-1})\omega_{0(1)}$, for odd (even) k , and $\vec{\sigma}$ are the Pauli matrices.

An alternative strategy for qubit control is to use classical driving fields. Resonant driving along a desired rotation axis achieves time-optimal steering of the qubit in the xy plane [12, 16]. Even when the direct driving of the qubit is slow, the rate might be increased by virtual transition of the actuator. This is the case for nuclear spins: while their coupling to an external driving field is weak, indirect forbidden transitions mediated by the electronic spin can considerably enhance the driving strength [17–19]. This nuclear Rabi enhancement depends on the state of the electronic spin. The effective Rabi frequency Ω for an isolated nuclear spin, hence, is modified from its bare value $\bar{\Omega}$ by the enhancement factors $\zeta_{0,\pm 1}$, corresponding to the electronic spin states $|0\rangle, |\pm 1\rangle$. The enhancement is proportional to the ratio of the qubit and actuator coupling to the external field. For nuclear and electronic spins considered here, $\gamma_e/\gamma_n \approx 2600$ and the effective Rabi frequencies $\Omega_i = (1 + \zeta_i)\bar{\Omega}$ can be much larger than the bare frequency.

We assume $\bar{\Omega} \approx 100\text{kHz}$ as an upper-limit on realistic bare nuclear Rabi frequencies by considering data in [20], where the ^{13}C considered was only weakly coupled and thus no Rabi enhancement was present. To achieve this strong driving, a dedicated microfabricated coil was necessary [21]. Rabi frequencies $\bar{\Omega} \approx 20\text{kHz}$ are, in our experience, in the upper achievable range with modest amplifiers and a simple wire to deliver the rf field.

Both regimes of $\kappa \lesseqgtr \cos(\alpha)$ for the time-optimal solutions can be explored in the NV center system by considering the coupling to ^{13}C at different distances from the NV defect [22–24]. The hyperfine tensors for ^{13}C located up to $\approx 8\text{\AA}$ away from the NV center were estimated using density functional theory [25]. In what follows, we numerically compare the performance of the proposed control method against direct driving under diverse experimental conditions and for a number of distinct nuclear spins. For the NV center system the dependence on the hyperfine parameters of both the actuator scheme time and the direct driving strength yields a broad variation of results for both close-by and more far away nuclei; while a trend toward longer times for the actuator scheme vs. direct driving is apparent as the distance from the NV center increases, the large variations indicate that the best scheme should be evaluated for individual nuclear spins.

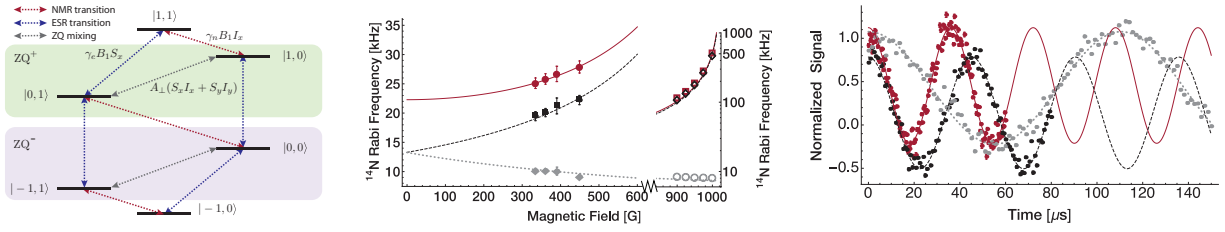


Fig. 2: Left: energy levels of the reduced NV- ^{14}N spin system, showing the transitions that are mixed by the transverse hyperfine coupling. Center: ^{14}N Rabi Frequency in the three NV manifold (Red, solid line $m_s = 0$. Black, dashed line, $m_s = -1$. Gray, dotted line $m_s = +1$) as a function of the magnetic. The filled symbols correspond to the experimental data, which matches closely the theoretical prediction. The effective Rabi frequencies increase rapidly with the field, exceeding 1MHz when close to ground state level anti-crossing. The enhancement allows fast manipulation of the nuclear spin even when the bare Rabi field is only $B_1 \approx 3\text{G}$. The theoretical prediction is confirmed by simulations (open symbols) of the spin dynamics. Right: ^{14}N Rabi oscillations at $B = 450\text{G}$ in the three NV manifold (Red, solid line $m_s = 0$. Black, dashed line, $m_s = -1$. Gray, dotted line $m_s = +1$). Here the dots are the experimental results, while the lines are fits to cosine oscillations. The different baseline of the $m_s = -1$ curve is due to small differences in the fluorescence emission of different nuclear manifolds.

Indirect control of qubits by a quantum actuator is an attractive strategy in many situations when the qubits couple weakly to external fields, but interact more strongly to another quantum system.

An interesting extension of our results would be to *simultaneously* control two or more qubits by the same quantum actuator. While this is possible, provided the qubits are coupled with different strengths [10], it becomes more difficult to find time-optimal solutions except for particular tasks (such as state-to-state transformations [26]) or geometries [27, 28]. Still, even when the goal is to control a larger number of qubits, our results can guide the experimentalist's choice between direct driving and the actuator control, for which these results give an upper bound.

2.2 Hybrid control: direct driving enhanced by a quantum actuator

When both direct driving and a quantum controller are available, one can take advantage of both to achieve faster driving of the qubit. In particular, we found that the quantum actuator can mediate virtual transitions that enhance the direct driving strength. In turn, since the enhancement depends on the actuator/register coupling strength, the enhancement can be used to precisely measure the coupling itself [3]. Precise knowledge of a system's Hamiltonian is a pre-requisite for its accurate control.

The NV ground state is a two-spin system given by the electronic spin of the NV center ($S = 1$) and the nuclear spin ($I = 1$) of the substitutional ^{14}N adjacent to the vacancy that comprise the defect. In the experiments, we are only interested in two of the nuclear spin levels ($m_I = +1, 0$) that we drive on-resonance, while the third level can be neglected. Then, the Hamiltonian of the reduced system is given by $\mathcal{H} = \mathcal{H}_{\parallel} + \mathcal{H}_{\perp}$, where the secular, \mathcal{H}_{\parallel} , and nonsecular, \mathcal{H}_{\perp} , terms are:

$$\begin{aligned}\mathcal{H}_{\parallel} &= \Delta S_z^2 + (\gamma_e B_z + \frac{A_{\parallel}}{2}) S_z + (Q + \gamma_n B_z) I_z + A_{\parallel} S_z I_z, \\ \mathcal{H}_{\perp} &= \sqrt{2} A_{\perp} (S_x I_x + S_y I_y).\end{aligned}\quad (8)$$

Here S and I are the electron spin-1 and nuclear spin-1/2 operator respectively, $\Delta = 2.87\text{ GHz}$ is the zero-field splitting and $Q = -4.945\text{ MHz}$ [29] the nuclear quadrupolar interaction. The NV spin is coupled to the nuclear spin by a hyperfine interaction with a longitudinal component $A_{\parallel} = -2.162\text{ MHz}$ [29] and a transverse component A_{\perp} which we want to estimate. A magnetic field B_z is applied along the NV crystal axis [111] to lift the degeneracy of the $m_s = \pm 1$ level, yielding the electron and nuclear Zeeman frequencies $\gamma_e B_z$ and $\gamma_n B_z$ where $\gamma_e = 2.8\text{ MHz/G}$ and $\gamma_n = 0.308\text{ kHz/G}$.

Let $|m_s, m_I\rangle$ be eigenstates of \mathcal{H}_{\parallel} . The transverse coupling A_{\perp} mixes states connected via zero-quantum (ZQ) transitions, $|+1, 0\rangle \leftrightarrow |0, 1\rangle$ and $|0, 0\rangle \leftrightarrow |-1, 1\rangle$. Thus, diagonalization of the total Hamiltonian

can be achieved by rotating the two ZQ subspaces with a unitary transformation $U_{ZQ} = e^{-i(\sigma_y^- \theta^- + \sigma_y^+ \theta^+)}$, where the rotation operators are given by $\sigma_y^+ = i(|+1, 0\rangle\langle 0, 1| - |0, 1\rangle\langle +1, 0|)$; $\sigma_y^- = i(|0, 0\rangle\langle -1, 1| - |-1, 1\rangle\langle 0, 0|)$ and the rotation angles are

$$\tan(2\theta^+) = \frac{2A_{\perp}}{\Delta + \gamma_e B_z - \gamma_n B_z - Q} \quad (9)$$

$$\tan(2\theta^-) = \frac{-2A_{\perp}}{\Delta - \gamma_e B_z - A_{\parallel} + \gamma_n B_z + Q}. \quad (10)$$

Because of this level mixing, a field on resonance with the nuclear spin transition also drives electronic transitions. Although the electronic spin state is unchanged to first order, as long as the mixing is small, the forbidden transitions result in an enhancement of the nuclear state driving frequency, as we explain below.

When applying a radio frequency (RF) field to drive the nuclear spin, the interaction Hamiltonian of the NV- ^{14}N system with the RF field is:

$$\mathcal{H}_{\text{rf}}(t) = 2B_1 \cos(\omega t)(\gamma_e S_x + \sqrt{2}\gamma_n I_x), \quad (11)$$

where B_1 is the RF field strength. The Hamiltonian can be simplified by going into a rotating picture at the RF frequency ω and applying the rotating wave approximation (RWA), to obtain $\mathcal{H}_{\text{rf}} = B_1(\gamma_e S_x + \sqrt{2}\gamma_n I_x)$. We note that since we might have $\gamma_e B_1 \gg \omega$, effects from the counter-rotating fields, such as Bloch-Siegert shifts of the electronic energies, might be present. These effects were however negligible at the fields and Rabi strengths used in the experiments. Transforming \mathcal{H}_{rf} with the unitary U and denoting the states and operators in the new frame by a hat, we obtain $\hat{\mathcal{H}}_{\text{rf}} = U_{ZQ}\mathcal{H}_{\text{rf}}(t)U_{ZQ}^{\dagger} = \mathcal{H}_n + \mathcal{H}_e$, with

$$\mathcal{H}_n = \gamma_n B_1 (\alpha_1 |\hat{1}\rangle\langle \hat{1}|_e + \alpha_0 |\hat{0}\rangle\langle \hat{0}|_e + \alpha_{-1} |-\hat{1}\rangle\langle -\hat{1}|_e) \hat{I}_x \quad (12)$$

Here α_{m_s} denote the enhancement factors in each manifold of the NV spin:

$$\alpha_{+1} \approx 1 + \frac{\gamma_e}{\gamma_n} \frac{A_{\perp}}{\Delta + \gamma_e B_z - \gamma_n B_z - Q}; \quad (13)$$

$$\alpha_0 \approx 1 - \frac{\gamma_e}{\gamma_n} \left(\frac{A_{\perp}}{\Delta + \gamma_e B_z - \gamma_n B_z - Q} + \frac{A_{\perp}}{\Delta - \gamma_e B_z - A_{\parallel} + \gamma_n B_z + Q} \right); \quad (14)$$

$$\alpha_{-1} \approx 1 + \frac{\gamma_e}{\gamma_n} \frac{A_{\perp}}{\Delta - \gamma_e B_z - A_{\parallel} + \gamma_n B_z + Q}, \quad (15)$$

where we show expressions exact up to the first order in θ^{\pm} (see [3] for the exact expressions). The Hamiltonian \mathcal{H}_e can be neglected since electronic spin transitions are far off-resonance.

To confirm the expected dependence of the Rabi enhancement factors on the external magnetic field and the NV state, we measured the Rabi oscillations at the three electronic spin manifolds with varying magnetic field B_z . As shown in Fig. (2), the measured Rabi frequencies match well with the theoretical model. It is worth noting that contrary to the static pseudo-nuclear Zeeman effect [30], there is a large enhancement ($\alpha_0 \sim 16$, $\alpha_{\pm 1} \approx -9$) even at zero field. Also, close to the ground state avoided crossing ($B \approx 0.1$ T) the enhancement can become very large, exceeding 100. The validity of our approximation in this regime can be confirmed by numerical simulations, based on Trotter expansion and Floquet theory. Thanks to the strong dependence of the enhancement factors from the transverse hyperfine coupling, we can determine A_{\perp} from measurement of the ^{14}N Rabi oscillations with higher precision than ever done previously, even in ensemble measurements.

2.3 Quantum Feedback

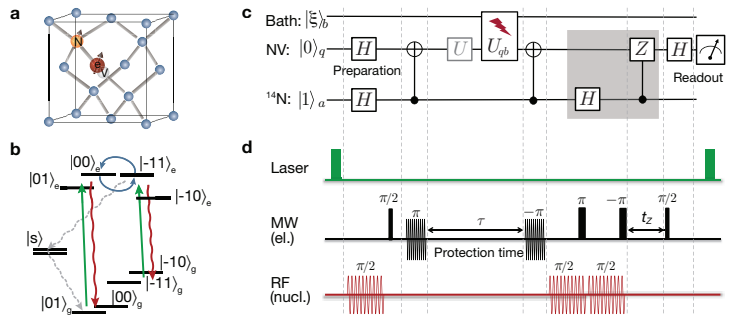
Engineering desired operations on qubits subjected to the deleterious effects of their environment is a critical task in quantum information processing, quantum simulation and sensing. The most common approach is to rely on open-loop quantum control techniques, including optimal control algorithms, Lyapunov design and Hamiltonian engineering [1]. An alternative strategy, inspired by the success of classical control, is feedback control. Because of the complications introduced by quantum measurement, closed-loop control is less pervasive in the quantum settings and its experimental implementations have been mainly limited to quantum optics experiments. We implemented a feedback control algorithm with a solid-state spin qubit system associated with the Nitrogen Vacancy (NV) centre in diamond, using coherent feedback to overcome limitations of measurement-based feedback (see Fig. 7), and show that it can protect the qubit against intrinsic dephasing noise for milliseconds (Fig. 4).

In coherent feedback, the quantum system is connected to an auxiliary quantum controller (ancilla) that acquires information about the system's output state (by an entangling operation) and performs an appropriate feedback action (by a conditional gate). In contrast to open-loop dynamical decoupling (DD) techniques, feedback control can protect the qubit even against Markovian noise and for an arbitrary period of time (limited only by the ancilla coherence time), while allowing gate operations. It is thus more closely related to Quantum Error Correction schemes, which however require larger and increasing qubit overheads. Increasing the number of fresh ancillas allows protection even beyond their coherence time as well as protection against multi-axis noise.

We further evaluated the robustness of the feedback protocol, which could be applied to quantum computation and sensing, by exploring an interesting tradeoff between information gain and decoherence protection, as measurement of the ancilla-qubit correlation after the feedback algorithm voids the protection, even if the rest of the dynamics is unchanged.

Fig.3: Feedback algorithm and experimental implementation. (a) NV centre in diamond and (b) relevant energy levels of the spin system, showing polarisation processes under optical illumination [31]. (c) *Quantum circuit.*

Hadamard gates prepare and read out a superposition state of the qubit, $|\varphi\rangle_q = \frac{1}{\sqrt{2}}(|0\rangle + |1\rangle)$. Amid entangling gates between qubit and ancilla, the qubit is subjected to noise (and possibly unitary gates U). We assume the ancilla



is not affected by the bath, yielding $\mathbf{1}_a \otimes U_{qb}(\tau)$, with $U_{qb}(\tau)$ the qubit-bath joint evolution. Given a dephasing bath, we set the entangling gate to $U_c = \sigma_x$ (conditional-NOT gate). More generally, upon undoing the entangling operation, the system is left in the state $|\Psi(\tau)\rangle = \frac{1}{\sqrt{2}}(|0\rangle_a K^+ |\varphi_q, \xi_b\rangle + |1\rangle_a K^- |\varphi_q, \xi_b\rangle)$, with $K^\pm = U_{qb} \pm U_c U_{qb} U_c^\dagger$. The entangling gate U_c is designed such that $K^+ = \mathbf{1}_q \otimes \chi_b^+$ and $K^- = U_q^\dagger \otimes \chi_b^-$, where χ_b^\pm act on the bath only, and U_q on the qubit. After measuring the ancilla, we could use a feedback operation U_q to restore the correct qubit state. The ancilla measurement is replaced by coherent feedback (shaded region) obtained by a controlled-correction gate (here $U_q = \sigma_z$ for dephasing noise). The final state of the combined system is then $\frac{1}{\sqrt{2}}(|0\rangle_a \chi_b^+ + |1\rangle_a \chi_b^-) |\varphi_q\rangle |\xi_b\rangle$, which reveals how the qubit is now decoupled from the bath.

(d) *Experimental implementation.* The laser excitation polarises both spins. Black sinusoidal lines refer to selective MW pulses acting only in the $m_I = 1$ manifold (thus mimicking controlled-NOT gates), while solid bars indicate non-selective pulses. The RF excitation describes selective pulses in the $m_s = 0$ manifold. We use $\pi/2$ rotations about x to approximate Hadamard gates. To implement a nonselective RF $\pi/2$ gate on the nuclear spin we embed a nonselective MW π pulse into two consecutive RF $\pi/2$ pulses. The controlled-correction gate is implemented by free evolution (t_Z) under hyperfine coupling.

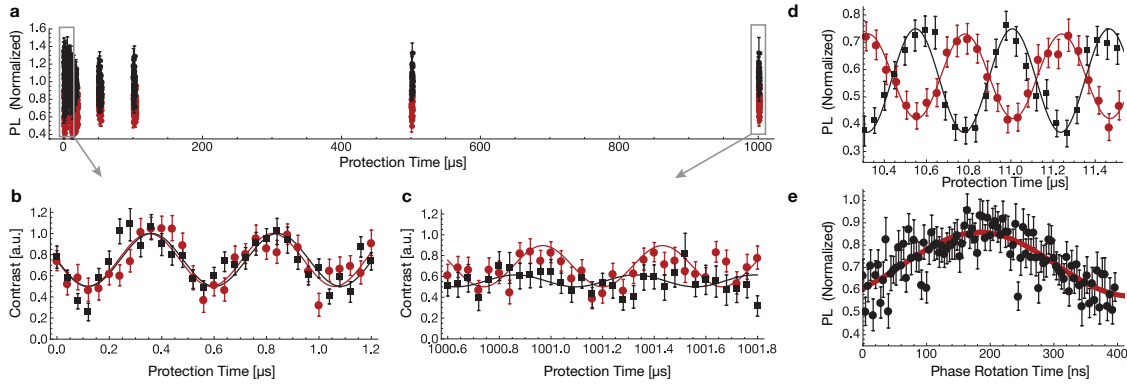


Fig. 4: Experimental demonstration of the feedback-based protection algorithm. (a) The signal –normalised Photoluminescence (PL) intensity– oscillates at the hyperfine coupling frequency, $A = -2.15$ MHz. The initial coherent superposition state of the qubit is preserved for a time $\tau > 1$ ms at 390 G (red dots), while we observe a sharp decrease in the signal amplitude at 514 G (black squares), where correlations between the qubit and ancilla states are partly measured. This is evident in the lower panels, where we compare the fidelity at short (b), and long (c) times, for $B = 390$ G and 514 G. To highlight the differences while taking into account different PL intensities at the two fields, we normalised all the data so that at short times the signal has the same (maximum) contrast. (d) Protected NOT gate (red circles). Here we show that the coherence of the qubit is protected for a time longer than the dephasing time, $\tau > T_{2e}^*$, even when a NOT gate is applied. We compare the dynamics to the NOOP dynamics (black squares), clearly showing that the NOT gate inverts the state of the qubit, as signalled by the out-of-phase oscillations. (e) Weak measurement of the ancilla: normalised PL signal after a protection time $\tau = 8\mu\text{s}$, as a function of the ancilla measurement strength. In the experiment, we vary the ancilla measurement strength by changing the angle of the last controlled phase rotation gate.

The success of the feedback-based protection algorithm rests on the fact that the increased qubit entropy, due to the coupling to the environment, is dumped on the ancilla. This could be revealed by measuring the state of the ancilla, which would yield information about the noise, while preserving the qubit state. If instead information about the ancilla is collected by a correlated qubit-ancilla measurement, the protection fails [32], as it would happen in a measurement-based feedback for an imperfect ancilla readout. We thus investigated this tradeoff between the protection power and information gain on the ancilla. We transferred a part of the ancilla entropy back to the qubit by employing a conditional gate that maps the state of the ancilla onto the qubit, correlating the two qubit states. By changing the angle of rotation of the conditional gate we can vary the strength of the ancilla measurement, from a weak measurement to a strong one. As more information about the ancilla is acquired, the fidelity of the protection gate decreases (Fig. 4b). Note that we can combine the conditional gate performing the weak measurement of the ancilla state with the last conditional Z-gate of the algorithm, thus in practice performing a conditional phase-shift gate. The qubit fidelity is maximised when the conditional gate performs the required π -rotation on the qubit, whereas it decreases when a different phase rotation is employed.

Our results provide important information about the robustness of quantum feedback.

3 Spin wires for quantum information transfer

The development of small quantum registers must be complemented by a strategy to couple them. Thus, the second activity of the program explored quantum information transfer using quantum spin wires, which transport information via the free evolution under their mutual interaction.

In this project we theoretically studied conditions for perfect quantum state transfer and we investigated an experimental implementation with nuclear magnetic resonance techniques applied to apatite crystals. We further studied the effects of decoherence on spin transport and we the performance of decoupling techniques in counteracting the effects of a spin bath. In addition, we looked at different experimental systems that could provide a platform for quantum information transport.

Achieved results include:

- We performed the first experimental implementation of quantum information transfer in mixed-state spin chains.
- We studied the coherence properties of highly correlated spin states under the effects of a correlated noise. We found that the restriction to one-dimensional geometries brings both a complex, non-Markovian dynamics and also longer coherence times than in 3D systems, thus pointing to advantages to be found in particular geometries for larger quantum information architectures.
- We investigated the effect of dephasing and depolarizing noise on quantum state transfer. For this study, we devised multi-pulse control sequences that re-introduce in a controlled way the effects of a spin bath onto the spin chains. This allows us to engineer different spin-bath effects
- We studied the polarization transfer from NV centers in diamond (that can be polarized optically) to dark spins associated with single Nitrogen defects (P1 centers) in diamond. We are now studying the polarization dynamics in the P1 spin system, with the goal of assessing its potential as a bus for quantum information transfer.

Details of these activities are described below.

3.1 Experimental implementation of quantum information transfer

We used nuclear spin systems in apatite crystals as a test-bed to probe quasi-one-dimensional (1D) dynamics, including transport and decoherence, and in particular to study protocols for quantum information transport. The crystal structure of fluorapatite [$\text{Ca}_5(\text{PO}_4)_3\text{F}$, FAp] and hydroxylapatite [$\text{Ca}_5(\text{PO}_4)_3(\text{OH})$, HAp] presents a favorable geometry where ^{19}F or ^1H nuclear spins are aligned in linear chains along the crystal c-axis with inter-spin spacings much shorter than the distance to other parallel chains. The system thus acts as an ensemble of linear spin chains with well characterized internal Hamiltonian. NMR techniques enable the exploration of quantum transport even in the absence of single-spin addressing and readout. We used a superconducting magnet (Oxford instrument, 7 T, wide-bore) and a spectrometer (Bruker Avance300 DMX) to control the nuclear spin system. The spectrometer is optimized for solid-state systems, achieving high-power pulses (300 W amplifiers) to address the broad linewidth of solid-state crystals as well as fast acquisition.

While an Hamiltonian for quantum state transfer can be relatively easily obtained with multiple quantum sequences, it is more challenging to initialize and readout the system in the absence of single-spin addressability. Thus, we first focused on these tasks.

The aim was to initialize the spin(s) at the end of the chain in a state of interest for the transfer of either classical or quantum information, while leaving the rest of the spin chain in the maximally mixed state. In the first case, we would like to prepare the state $\delta\rho_z^1 \sim \sigma_z^1 \otimes \mathbb{1}$; whereas in the second case we would like to prepare one of the logical states, e.g., $\delta\rho_y^L = \frac{\sigma_y^1\sigma_x^2 + \sigma_x^1\sigma_y^2}{2} \otimes \mathbb{1}_{n-2}$ [5]. Exploiting the spin natural dynamics and a combination of coherent and incoherent control it is possible not only to prepare, but even to detect

these types of states [5]. This was one critical step toward the demonstration of QST in a solid-state NMR platform.

The key insight was to realize that even in the absence of frequency addressability, the dynamics of the end-chain spins under the internal dipolar Hamiltonian is different from the bulk spins, as the end-spins have only one nearest neighbor.

Polarization initially in the transverse plane, $\delta\rho = \sum_{k=1}^N \sigma_x^k$ (prepared from the thermal state by a $\pi/2$ pulse), evolves under the internal dipolar Hamiltonian at different rates. The end-spin evolution rate is slower by a factor $\approx 1/\sqrt{2}$ as compared to the rest of the chain, due to fewer numbers of couplings with neighboring spins. Thus, there exist a time t_1 when the state of the end-spins is still mainly σ_x , whereas the rest of the spins have evolved to many-body correlations. A second $\pi/2$ pulse brings the end-spin magnetization back to the longitudinal axis, while an appropriate phase cycling scheme cancels out other terms, thus obtaining the state

$$\delta\rho_{end} = \delta\rho_z^1 + \delta\rho_z^N. \quad (16)$$

We note that the chain geometry prevents breaking the symmetry between spin 1 and N . Here the phase cycling achieves a similar result of temporal averaging in the preparation of pseudo-pure states. The sequence that prepares this state can thus be written as

$$\frac{\pi}{2} \Big|_{\alpha} \text{---} t_1 \text{---} \frac{\pi}{2} \Big|_{-\alpha}, \quad (S1)$$

with $\alpha = \{-x, y\}$, to average out terms that do not commute with the total magnetization $\Sigma_z = \sum_k \sigma_z^k$. As the phase cycling does not cancel zero-quantum coherences, they will be the main source of errors in the initialization scheme.

A similar control strategy can be as well used to read out the spins at the end of the chain even if the observable in inductively measured NMR is the collective magnetization of the spin ensemble, Σ_z .

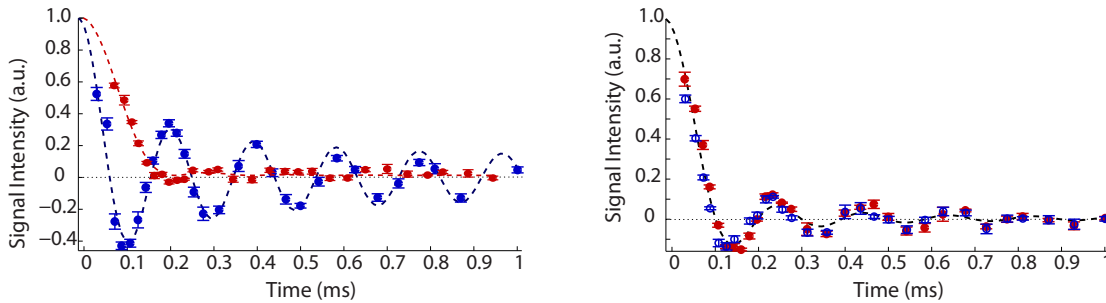


Fig. 5: Transport under the DQ Hamiltonian [5]. Data points are the experimental data, with error bars obtained from the offset of the signal from zero. The lines are the fits using the analytical model. The fitting. LEFT: Blue: Initial state $\delta\rho_{th}$; readout, collective magnetization, Σ_z . Red: Initial state, $\delta\rho_{end}$; readout, end readout. The two curves highlight the differences arising from the different initial state and readouts. RIGHT: Blue, open circles: Initial state, $\delta\rho_{end}$; readout, collective magnetization, Σ_z . Red, filled circles: Initial state, $\delta\rho_{th}$; readout, end-spin readout. The experimental data shows remarkable agreement between the two schemes, thus confirming the validity of the initialization and readout methods.

To measure a different observable, the desired state must be prepared prior to acquisition. Thus we want to turn Σ_z into the end-chain state, Eq. (16). In general, the sequence used for readout cannot be a simple inversion of the end-selection step since this is not a unitary –reversible– operation. It is however sufficient to ensure that the state prior to the end-selection sequence has contributions mainly from population terms ($\propto \sigma_z^k$) for the sequence (S1) to work as a readout step. Since the states created by evolution under the DQ Hamiltonian are already of the form $\propto \sigma_z^k$, the (S1) sequence with a two-step phase cycling is enough for the end-readout step.

We verified the effectiveness of the initialization and readout methods by probing the transport dynamics driven by the transport Hamiltonian, comparing the end-polarized states and observables with the thermal-equilibrium state. In the timescale of the experiment, the initial perturbation travels across ≈ 17 spins, however only polarization leaving one end of the chain could be observed: a clear signature of the polarization reaching the other end is erased by the distribution of chain lengths. Still, the experimental verification of initial state preparation is possible even at these short time scales thanks to marked differences in the signal arising from the evolution of thermal and end-polarized states under DQ Hamiltonian.

The left panel of figure (5) (blue) shows the observed evolution of the collective magnetization Σ_z under the DQ Hamiltonian, starting from the thermal initial state, $\delta\rho_{th} = \Sigma_z$. Modeling the physical spin system by an ensemble of equivalent and independent spin chains with nearest-neighbour couplings only, we can derive analytical formulas for the evolution to fit the experimental data, finding a very good agreement. The red data (5) show instead the evolution of the end polarized initial state under the transport Hamiltonian, measured using the readout strategies outlined above. This experiment is thus a direct simulation of quantum state transport. The two sets of data show very different chain dynamics for the two initial states (with and without end selection), giving an experimental validation of our initialization method.

To further validate the initialization and readout method, in the right panel of figure (5) (blue, open circles) we plot the system dynamics when starting from an end-polarized state (where polarization is localized at the ends of the chain) and reading out the collective magnetization. The red (filled circle) data shows a complementary measurement where we start from thermal initial state, given by the collective magnetization, and read out the ends of the chains after evolution under the DQ Hamiltonian. Both these data sets were fitted by the analytical expression that can be found in the nearest-neighbor coupling limit, thanks to a Jordan-Wigner transformation to non-interacting fermions. Furthermore, the data and fittings for end selection and end readout measurements are very similar. This indicates the robustness of the readout step.

We use the end-selection scheme not only to prepare the end-chain polarized states, but also the logical states required for quantum information transport. First we prepare the end polarized state $\delta\rho_{end}$ by the sequence (S1). Then this evolves under the DQ Hamiltonian for a very short time $t_{DQ} = 14.7\mu s$, thus creating a two-spin correlated state as required. We can write this initialization sequence as

$$\frac{\pi}{2} \Big|_{\alpha} - t_1 - \frac{\pi}{2} \Big|_{\beta} - \text{DQ}^{\gamma}, \quad (\text{S2})$$

where $\text{DQ}^{\gamma=x}$ is propagation under $U_{MQ}(t_{DQ}) = e^{-i\bar{H}_{DQ}t_{DQ}}$ and $\text{DQ}^{\gamma=y}$ under U_{MQ}^{\dagger} . Setting $[\alpha, \beta, \gamma] = [-x, x, x]$, the state after the sequence (S2) is approximately given by zero and double quantum coherences, $\delta\rho_{end}(t_{DQ}) \approx \sigma_{1,2}^{zq} + \sigma_{n-1,n}^{zq} + \sigma_{1,2}^{\text{DQ}} + \sigma_{n-1,n}^{\text{DQ}}$, where $\sigma_{i,j}^{zq} = (\sigma_x^i \sigma_y^j - \sigma_y^i \sigma_x^j)$ and $\sigma_{i,j}^{\text{DQ}} = (\sigma_x^i \sigma_y^j + \sigma_y^i \sigma_x^j)$.

A double quantum filter given by the four-step phase cycling scheme,

$$[\alpha, \beta, \gamma] = \{[-x, x, x]; [y, -y, x]; [-x, -x, y]; [y, y, y]\}$$

cancels out the zero-quantum terms and selects the double-quantum terms, which is our desired state: $\delta\rho_y^L \propto$

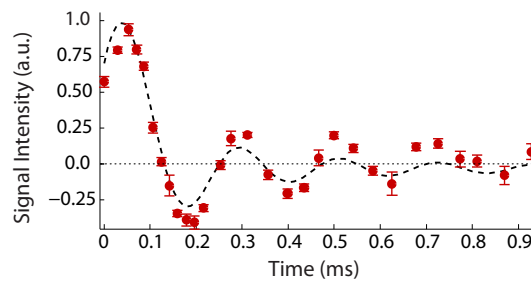


Fig. 6: Evolution of the logical state $\delta\rho_y^L$ under the transport Hamiltonian, first reported in [5]. The logical initial state was prepared using the sequence (S2) and its evolution under the DQ Hamiltonian monitored by observing the collective magnetization. Circles represent the experimental data; and the dashed line is the fit to the analytical model.

$\sigma_{1,2}^{\text{DQ}} + \sigma_{n-1,n}^{\text{DQ}}$. Figure (6) shows the evolution of this state under the DQ Hamiltonian while the dynamics was monitored by measuring the collective magnetization, $S^L \propto \text{Tr} \left\{ U_{\text{MQ}} \delta \rho_y^L U_{\text{MQ}}^\dagger \sigma_z \right\}$. We note that this experiment implements the transport of quantum information via a maximally mixed quantum channel.

3.2 Decay of spin coherences in one-dimensional spin systems

While working to build the control tools to realize large scale quantum information architectures, we also investigated their coherence properties [6], as multi-qubit systems in correlated and entangled states are usually more fragile to decoherence. We experimentally studied the decay of such multi-qubit states under the action of a correlated spin bath, investigating the decay rate dependence on the correlations in a multi-qubit spin state. We leveraged the low dimensionality of the system studied – the linear coupling geometry provided by nuclear spins in apatite crystals – to gain insight into both the many-body states created by the coherent Hamiltonian dynamics and their subsequent decay. We were thus able to derive a simple analytical model that captures the essential features of the multi-qubit decays, and compares well with the experimental data. These results will be helpful in paving the way for the future design of schemes to mitigate the decay. The experimental scheme is shown in Fig. 7. The system is first prepared in a suitable initial state ρ_i . Evolution under a propagator U_{MQ} for a time τ creates a complex, multiple-quantum coherence state. The system is then let evolve freely for a time t , during which the coherences decay mainly under the effects of the dipolar Hamiltonian. In order to observe this decay, we first refocus the remaining coherences with a propagator U_{MQ}^\dagger before measuring the spin magnetization via the usual free induction decay.

We created spin correlations by evolution under the double quantum (DQ) Hamiltonian

$$\mathcal{H}_{\text{DQ}} = \sum_{ij} b_{ij} (\sigma_x^i \sigma_x^j - \sigma_y^i \sigma_y^j), \quad (17)$$

which is known to generate quantum coherences among the spins. The density operator created by evolution under the DQ Hamiltonian can be decomposed into its multiple quantum coherences (MQC) components,

$$\rho(\tau) = U_{\text{MQ}}(\tau) \rho(0) U_{\text{MQ}}^\dagger(\tau) = \sum_m \rho^{(m)}, \quad (18)$$

where a multiple quantum term of order m , $\rho^{(m)}$, acquires a phase $m\varphi$ under a collective Σ_z rotation by an angle φ . The correlated spin states created under \mathcal{H}_{DQ} evolution contain in general all *even* M coherence orders. However, since standard NMR techniques measure only single-quantum coherences (SQC), in order to probe the higher spin coherences it is necessary to indirectly encode their signatures into SQCs which can be measured inductively. This is achieved by labeling each coherence order with a different phase φ by means of collective rotations $U_\varphi = \exp(-i\varphi \Sigma_z / 2)$ about the z axis, effectively creating the phase shifted DQ Hamiltonian, $\mathcal{H}_{\text{DQ}}^\varphi = U_\varphi \mathcal{H}_{\text{DQ}} U_\varphi^\dagger$. Finally, MQC are refocused back to single-spin single-quantum

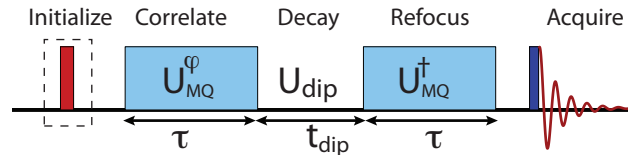


Fig. 7: Experimental scheme. The system is first prepared in an initial state of interest, for example the thermal equilibrium state or $\sum \sigma_x$ using a $\pi/2$ -pulse (red bar). Evolution via the DQ Hamiltonian \mathcal{H}_{DQ} (obtained by a multi-pulse sequence, blue rectangles) creates spin correlations during the time τ . A phase shift φ of the propagator encodes information about the multiple quantum coherence intensities created. The state undergoes decay under the dipolar interaction \mathcal{H}_{dip} during the time t . The correlated state is refocused by the inverse propagator U_{DQ}^\dagger before a $\pi/2$ pulse is used to detect the spin free-induction decay.

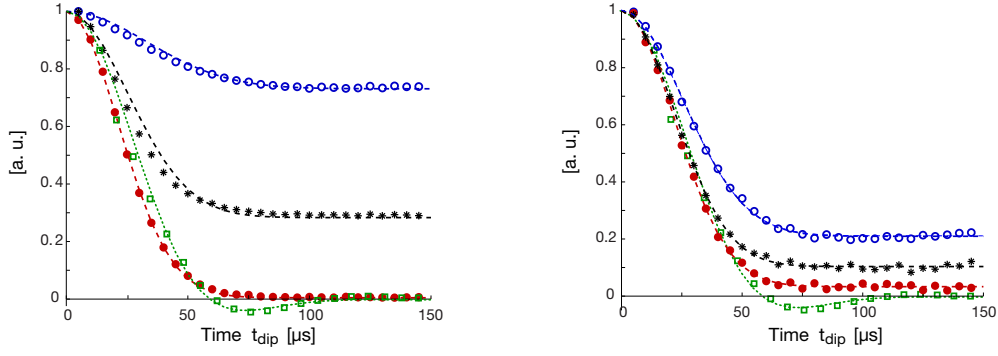


Fig. 8: Normalized decay of quantum coherences created from the thermal initial state by evolving for a time τ under the \mathcal{H}_{DQ} Hamiltonian. (ZQ (0Q) blue open circles, DQ (2Q) red dots, Total signal black stars). Data points are the normalized signal intensities for evolution time $48\mu\text{s}$ (left) and $589\mu\text{s}$ (right). The dashed lines are fitting using the function in Eq. 20. For comparison we plot the free induction decay (green squares) that we fit with the function $A \left[(1 - C)\text{sinc}(m_2 t) e^{-m_1 t^2/2} + C \right]$, with the second moment given by $M = m_1 + m_2^2/3$.

terms and free induction decay is measured. Each measurement is repeated while incrementing φ from 0 to 2π in steps of $\delta\varphi = 2\pi/2K$ where K is the highest order of MQC we wish to encode.

Since often the observable $\delta\rho_o$ is proportional to the initial state (as it is the case for the thermal equilibrium state and the total magnetization along the z-axis) we can write the measured signal as a correlation $S(t, \tau) = \text{Tr} \{ \delta\rho(t, \tau) \delta\rho_o(\tau) \}$, between the state prepared by the DQ evolution, $\delta\rho_o(\tau) = U_{\text{MQ}}(\tau) \delta\rho_o U_{\text{MQ}}^\dagger(\tau)$ and the same state after decay under the dipolar evolution, $\delta\rho(t, \tau) = U_{\text{dip}} \delta\rho_o(\tau) U_{\text{dip}}^\dagger$. The signal intensities of various coherence orders are given by the Fourier Transform with respect to the phase φ :

$$I^{(m)}(t, \tau) = \text{Tr} \left\{ \delta\rho_o^{(m)}(\tau) \delta\rho^{(m)}(t, \tau) \right\} = \sum_{k=1}^K S^k(t, \tau) e^{-ikm\delta\varphi}, \quad (19)$$

where $S^k(t, \tau) = \text{Tr} \left\{ \delta\rho_f^k(t, \tau) \delta\rho_o \right\}$ is the signal acquired in the k th measurement when setting $\varphi = \pi k/K$. We studied the decay of MQC intensities created under \mathcal{H}_{DQ} starting from an initial thermal state ($\delta\rho_{th} \sim \Sigma_z$) and other states of interest (end-polarized states and transverse polarization states). The decoherence dynamics was studied by repeating the experimental scheme described above while varying the DQ evolution time (τ) from $36\mu\text{s}$ to $925\mu\text{s}$ and the decay time (t) from 0 to $145\mu\text{s}$ (which is on the order of the free induction decay time).

We fitted the decay curves to Gaussian functions,

$$G(t, \tau) = A(\tau) \left([1 - C(\tau)] e^{-M(\tau)t^2/2} + C(\tau) \right), \quad (20)$$

where A (amplitude), M (second moment) and C (asymptote) are used as fitting parameters that vary with the DQ time τ . As shown by the behavior of the fitting parameters in Fig. 9, the system exhibits an interesting dynamics as a function of the DQ-time evolution. This is in contrast to what was observed in 3D systems, where the decay simply becomes monotonically faster as the DQ-time τ is increased. The difference can be traced to the fact that the constrained coupling topology in 1D systems allow for a slower decay dominated by nearest-neighbor interactions, while in 3D systems the decay is more rapid and diffusion-like.

We were able to derive an analytical model for the parameters of this decay, the asymptote C

$$C(\tau) = \left(\frac{1}{N} \sum_p (-1)^p f_{pp}(2\tau) \right)^2 = \left(\frac{1}{N} \sum_k \cos(4\tau \cos \kappa) \right)^2 \quad (21)$$

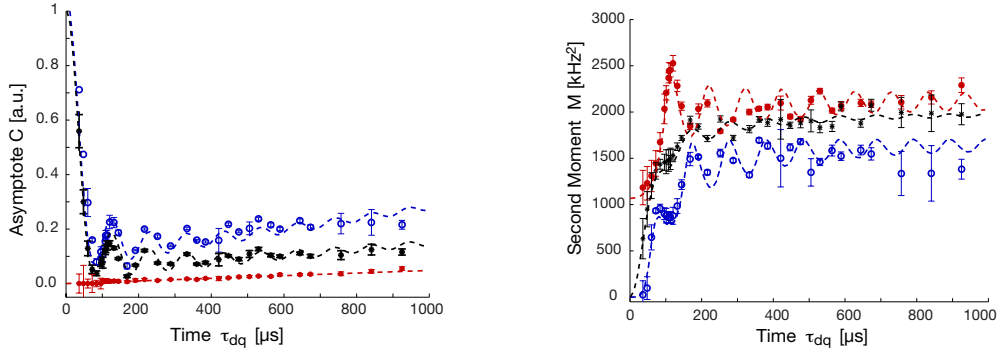


Fig. 9: Left: Asymptotes of the experimental decay curves (C_{ZQ} blue, C_{DQ} red C_{total} black). The curves were fitted by Eq. 21 with an additional linear term in τ , giving a dipolar coupling of $7.676 \times 10^3 \text{ rad/s}$. Right: Decay rates of the different MQ components as a function of double quantum evolution time τ . Points are experimental results obtained from the fitting of individual decay curves for each DQ-time τ . Error bars are estimated from fitting of decay curves with 20). The dashed lines are $\mu M(b, \tau)$, where $M(b, \tau)$ are the analytical curves.

and the decay moment $M = M_{zz} + 2M_{xx}$:

$$M_{zz} = \frac{16}{N} \left[\sum_{p \neq q} |f_{p,q}(2\tau)|^2 - \sum_{q=2}^N (|f_{q,q-1}(2\tau)|^2 + |f_{q,q-2}(2\tau)|^2 + |f_{1,q}(2\tau)|^2) \right], \quad (22)$$

$$M_{xx} = \frac{4(N-1)}{N} - \frac{2}{N} \sum_{p,q} [f_{p+1,q}(2\tau) - f_{p-1,q}(2\tau)] [f_{p,q+1}(2\tau) - f_{p,q-1}(2\tau)], \quad (23)$$

with

$$f_{pq}(\tau) = \frac{2}{n+1} \sum_k (-1)^p \sin(p\kappa) \sin(q\kappa) e^{-2ibt \cos \kappa}, \quad (24)$$

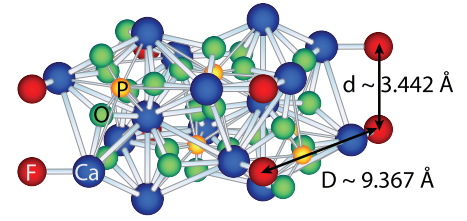
where N is the chain length and $\kappa = \frac{\pi k}{N+1}$. These expressions were obtained by approximating the Hamiltonian with a nearest-neighbor only interaction and using a mapping to non-interacting fermions.

We further investigated the dependence of decoherence rate for different initial states that evolve under the DQ-Hamiltonian to interesting many-spin states showing different types of spin-spin correlations. Since the decay process is non-Markovian, but it is due to a highly correlated spin bath, we found a very rich dynamics, where decoherence rates (quantified by the second moment of the the decay) depend in a non-trivial way on the degree of localization of the state as well as on its coherence with respect to the quantization basis. In particular we found that large spin clusters, with correlations established among many spins, decay faster under a correlated bath, even if their coherence order is not very large. This is in contrast to the decay under simple dephasing, where the coherence order (and for pure states, the entanglement) is critical in determining the decay rate. While it was not possible to separate the coherence order and the number of correlated spins in the dynamics of 3D spin systems (as they grow at the same time), here we were able to get more insight by using spin chains and exploring different initial states. In addition we found that restricting the dynamics in one dimension slows down the decay, which could be beneficial to create larger coherent quantum states.

3.3 Engineering Dephasing and Depolarizing Noise

In the first year of the project, we focused most of our efforts in devising strategies to achieve perfect quantum information transport by engineering the spin interactions. We found that dynamically modulating the spin-spin couplings could lead to perfect fidelity of information transfer even in disordered systems. However, these results could be voided if decoherence is at play [33]. Thus, we later focused our attention

Fig. 10: Unit cell of the fluorapatite crystal $[\text{Ca}_5(\text{PO}_4)_3\text{F}]$, highlighting the geometry of the fluorine chains (in red) and the phosphorus nuclei (in yellow). Each fluorine spin is surrounded by 3 phosphorus spins. As the phosphorus are in a thermal state, they create a local random magnetic field at the location of each fluorine spin that induces decoherence and localization unless the spins are decoupled by active control.



to studying effects of decoherence and disorder *during* the transport. To do so, we exploited the presence of a second nuclear species in our experimental system.

Fluorapatite crystals indeed contain phosphorus, whose nucleus ^{31}P has a spin-1/2 with gyromagnetic ratio $\gamma_P = 17.25\text{MHz/T}$ (compare to the fluorine's $\gamma_F = 40\text{MHz/T}$). While in previous experiments the system dynamics was protected against the fluorapatite ^{31}P spin bath, it is interesting to study what would be its effects on the transport dynamics. In particular, disorder and noise have been indicated as potential sources of localization, which would prevent the goal of transferring quantum information. The couplings to ^{31}P are weaker than F-F in-chain couplings, since the gyromagnetic ratio is smaller and distance is larger (the closest distance between a ^{19}F and a ^{31}P is 3.5\AA (compare to a distance 3.4\AA between Fluorines in the spin chains). However, since there are 3 ^{31}P per each ^{19}F , their combined effect is large, as indicated by calculations of the second moments. The ^{31}P nuclei act as a spin bath, coupling to the fluorine via the Hamiltonian

$$\mathcal{H}_{PF} = \sum_{jl} \frac{\gamma_P \gamma_F \hbar \mu_0}{4\pi} \frac{3 \cos(\vartheta_{jl})^2 - 1}{|r_{jl}|^3} I_{z,j}^P I_{z,l}^F$$

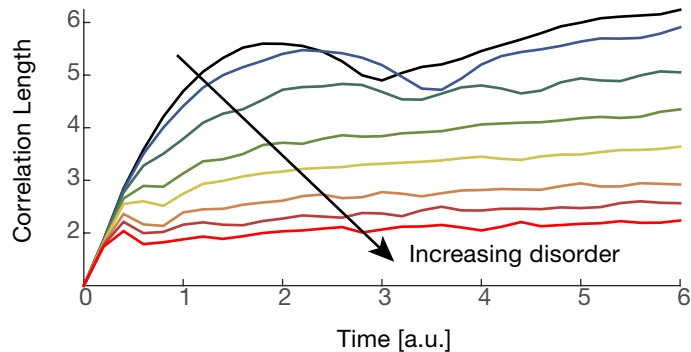
From the point of view of the fluorine spins, this amounts to the presence of a local magnetic field

$$B_P^j = \sum_j \frac{\gamma_P \gamma_F \hbar \mu_0}{4\pi} \frac{3 \cos(\vartheta_{jl})^2 - 1}{|r_{jl}|^3} \langle I_{z,j}^P \rangle$$

which depends on the (thermal) state of the phosphorus spins. In addition the ^{31}P interact among themselves, thus giving rise to a time-dependent magnetic field. Using multiple pulse sequences, we can engineer the ^{19}F dynamics (for example engineering the transport Hamiltonian \mathcal{H}_{DQ} while at the same time refocusing or shaping the spin bath interaction).

This allows us to study not only decoherence, but more importantly, the effects of a disorder onto the transfer of information. In particular, we are able to observe experimentally Anderson localization.

Fig. 11: Simulation of localization in spin chains due to a disordered magnetic field. Here we plot a measurable observable, the many-body correlation length, describing the average number of correlated spins. The correlation length can be measured experimentally from the multiple quantum coherence intensities.



3.4 Polarization Generation and Transfer in Electronic spin systems

In addition to nuclear spin chains in fluorapatite, we investigate an alternative spin system, connected to the NV center in diamond. While in diamond it is not yet possible to obtain regular arrays of spins, we still

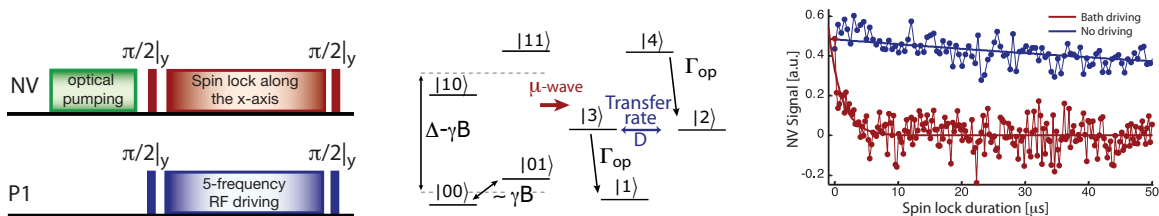


Fig. 12: Left: Hartmann-Hahn matching sequence for polarization contact. Right: Energy matching in the rotating (dressed) frame, here for two spin-1/2. Measured decay of NV spin-lock signal as a function of spin-lock duration. When the P1 bath is not driven we record the blue trace. Driving the P1 bath simultaneously at all 5 ESR resonances such that the collective P1 bath Rabi frequency equals the NV Rabi frequency (8 MHz) gives the red trace, indicating strong NV/P1 polarization transfer. Solid lines represent fits to decaying exponentials.

started investigating polarization transfer. This work laid the foundations for further experiments that will combine our results in control of local quantum registers and results in quantum information transfer with spin wires.

We investigated generation of polarization and its transport by exploiting the NV center in diamond as a source of polarization and the bath of electronic spins as the bus. The most common nitrogen defect in diamond is the P1 center, a nitrogen substitutional atom with an unpaired electron. The P1 center has electronic spin-1/2, with a strong hyperfine interaction with its nuclear spin giving rise to 5 distinct resonance frequencies. Polarization transfer between the NV center and other spins can be achieved by continuous irradiation at the Hartmann-Hahn matching condition [34]. The CW field effectively establishes a resonance condition in the rotating frame (or dressed basis).

As the NV spin can be polarized optically with high efficiency, the polarization can be transferred to the electronic spin bath. The transfer was implemented by achieving an energy matching between the NV and P1 spins in the rotating frame. We proved this mechanism experimentally, overcoming the difficulties associated with the large hyperfine of the P1 centers, which required us to simultaneously drive 5 resonance transitions [35]. The energy contact was confirmed by a reduction in the NV coherence time (Fig. 12).

References Cited

- [1] A. Ajoy and P. Cappellaro, “Quantum simulation via filtered hamiltonian engineering: application to perfect quantum transport in spin networks,” *Phys. Rev. Lett.*, vol. 110, p. 220503, 2013.
- [2] C. Aiello, M. Allegra, B. Hemmerling, X. Wan, and P. Cappellaro, “Algebraic synthesis of time-optimal unitaries in $su(2)$ with alternating controls,” *Quantum Inf. Process.*, vol. 14, no. 9, pp. 3233–3256, 2015.
- [3] M. Chen, M. Hirose, and P. Cappellaro, “Measurement of transverse hyperfine interaction by forbidden transitions,” *Phys. Rev. B*, vol. 92, p. 020101, Jul 2015.
- [4] M. Hirose and P. Cappellaro, “Coherent feedback control of a single qubit in diamond.” third round of review in *Nature*, 2015.
- [5] G. Kaur and P. Cappellaro, “Initialization and readout of spin chains for quantum information transport,” *New J. Phys.*, vol. 14, no. 8, p. 083005, 2012.
- [6] G. Kaur, A. Ajoy, and P. Cappellaro, “Decay of spin coherences in one-dimensional spin systems,” *New J. Phys.*, 2013.
- [7] M. Hirose and P. Cappellaro, “Time-optimal control with finite bandwidth,” *Arxiv:1510.06801*, 2015.

- [8] F. Ticozzi, R. Lucchese, P. Cappellaro, and L. Viola, “Hamiltonian control of quantum dynamical semigroups: Stabilization and convergence speed,” *IEEE TAC*, vol. 57, no. 8, pp. 1931–1944, 2012.
- [9] C. D. Aiello and P. Cappellaro, “Time-optimal control by a quantum actuator,” *Phys. Rev. A*, vol. 91, p. 042340, Apr 2015.
- [10] J. S. Hodges, J. C. Yang, C. Ramanathan, and D. G. Cory, “Universal control of nuclear spins via anisotropic hyperfine interactions,” *Phys. Rev. A*, vol. 78, no. 1, p. 010303, 2008.
- [11] N. Khaneja, “Switched control of electron nuclear spin systems,” *Phys. Rev. A*, vol. 76, no. 3, p. 032326, 2007.
- [12] U. Boscain and P. Mason, “Time minimal trajectories for a spin 1/2 particle in a magnetic field,” *J. Math. Phys.*, vol. 47, no. 6, p. 062101, 2006.
- [13] U. Boscain and B. Piccoli, *Optimal syntheses for control systems on 2-D manifolds*. Mathématiques & applications, Springer, 2004.
- [14] G. C. Hegerfeldt, “Driving at the quantum speed limit: Optimal control of a two-level system,” *Phys. Rev. Lett.*, vol. 111, p. 260501, Dec 2013.
- [15] M. W. Doherty, F. Dolde, H. Fedder, F. Jelezko, J. Wrachtrup, N. B. Manson, and L. C. L. Hollenberg, “Theory of the ground-state spin of the nv- center in diamond,” *Phys. Rev. B*, vol. 85, p. 205203, May 2012.
- [16] A. D. Boozer, “Time-optimal synthesis of su(2) transformations for a spin-1/2 system,” *Phys. Rev. A*, vol. 85, p. 012317, Jan 2012.
- [17] Bleaney in *Hyperfine interactions* (A. Freeman and R. Frankel, eds.), p. 1, Academic Press, 1967.
- [18] A. Abragam and B. Bleaney, *Electron Paramagnetic Resonance of Transition Ions*. Oxford University Press, Oxford, 2012.
- [19] L. Childress, M. V. Gurudev Dutt, J. M. Taylor, A. S. Zibrov, F. Jelezko, J. Wrachtrup, P. R. Hemmer, and M. D. Lukin, “Coherent dynamics of coupled electron and nuclear spin qubits in diamond,” *Science*, vol. 314, no. 5797, pp. 281–285, 2006.
- [20] P. C. Maurer, G. Kucsko, C. Latta, L. Jiang, N. Y. Yao, S. D. Bennett, F. Pastawski, D. Hunger, N. Chisholm, M. Markham, D. J. Twitchen, J. I. Cirac, and M. D. Lukin, “Room-temperature quantum bit memory exceeding one second,” *Science*, vol. 336, no. 6086, pp. 1283–1286, 2012.
- [21] N. Sun, Y. Liu, L. Qin, H. Lee, R. Weissleder, and D. Ham, “Small nmr biomolecular sensors,” *Solid-State Electronics*, vol. 84, no. 0, pp. 13 – 21, 2013.
- [22] A. Gali, M. Fyta, and E. Kaxiras, “Ab initio supercell calculations on nitrogen-vacancy center in diamond: Electronic structure and hyperfine tensors,” *Phys. Rev. B*, vol. 77, no. 15, p. 155206, 2008.
- [23] S. Felton, A. M. Edmonds, M. E. Newton, P. M. Martineau, D. Fisher, D. J. Twitchen, and J. M. Baker, “Hyperfine interaction in the ground state of the negatively charged nitrogen vacancy center in diamond,” *Phys. Rev. B*, vol. 79, p. 075203, Feb 2009.
- [24] A. Dréau, J.-R. Maze, M. Lesik, J.-F. Roch, and V. Jacques, “High-resolution spectroscopy of single nv defects coupled with nearby ^{13}C nuclear spins in diamond,” *prb*, vol. 85, p. 134107, 2012.
- [25] B. Smeltzer, L. Childress, and A. Gali, “ ^{13}C hyperfine interactions in the nitrogen-vacancy centre in diamond,” *New Journal of Physics*, vol. 13, p. 025021, Feb 2011.

- [26] E. Assémat, M. Lapert, Y. Zhang, M. Braun, S. J. Glaser, and D. Sugny, “Simultaneous time-optimal control of the inversion of two spin- $\frac{1}{2}$ particles,” *Phys. Rev. A*, vol. 82, p. 013415, 2010.
- [27] D. Burgarth, K. Maruyama, M. Murphy, S. Montangero, T. Calarco, F. Nori, and M. B. Plenio, “Scalable quantum computation via local control of only two qubits,” *Phys. Rev. A*, vol. 81, no. 4, p. 040303, 2010.
- [28] Y. Zhang, C. A. Ryan, R. Laflamme, and J. Baugh, “Coherent control of two nuclear spins using the anisotropic hyperfine interaction,” *Phys. Rev. Lett.*, vol. 107, p. 170503, Oct 2011.
- [29] B. Smeltzer, J. McIntyre, and L. Childress, “Robust control of individual nuclear spins in diamond,” *Phys. Rev. A*, vol. 80, p. 050302, Nov 2009.
- [30] A. Abragam and B. Bleaney, *Electron Paramagnetic Resonance of Transition Ions*. Clarendon Press, Oxford, 1970.
- [31] V. Jacques, P. Neumann, J. Beck, M. Markham, D. Twitchen, J. Meijer, F. Kaiser, G. Balasubramanian, F. Jelezko, and J. Wrachtrup, “Dynamic polarization of single nuclear spins by optical pumping of nitrogen-vacancy color centers in diamond at room temperature,” *Phys. Rev. Lett.*, vol. 102, no. 5, p. 057403, 2009.
- [32] Y.-H. Kim, R. Yu, S. P. Kulik, Y. Shih, and M. O. Scully, “Delayed “choice” quantum eraser,” *Phys. Rev. Lett.*, vol. 84, pp. 1–5, Jan 2000.
- [33] P. Cappellaro, “Implementation of state transfer hamiltonians in spin chains with magnetic resonance techniques,” in *Quantum State Transfer and Network Engineering* (G. M. Nikolopoulos and I. Jex, eds.), Quantum Science and Technology, pp. 183–222, Springer Berlin Heidelberg, 2014.
- [34] S. R. Hartmann and E. L. Hahn, “Nuclear double resonance in the rotating frame,” *Phys. Rev.*, vol. 128, pp. 2042–2053, 1962.
- [35] C. Belthangady, N. Bar-Gill, L. M. Pham, K. Arai, D. Le Sage, P. Cappellaro, and R. L. Walsworth, “Dressed-state resonant coupling between bright and dark spins in diamond,” *Phys. Rev. Lett.*, vol. 110, p. 157601, 2013.

1.

1. Report Type

Final Report

Primary Contact E-mail

Contact email if there is a problem with the report.

pcappell@mit.edu

Primary Contact Phone Number

Contact phone number if there is a problem with the report

6172538137

Organization / Institution name

Massachusetts Institute of Technology

Grant/Contract Title

The full title of the funded effort.

YIP: Modular Paradigm for Scalable Quantum Information

Grant/Contract Number

AFOSR assigned control number. It must begin with "FA9550" or "F49620" or "FA2386".

FA9550-12-1-0292

Principal Investigator Name

The full name of the principal investigator on the grant or contract.

Paola Cappellaro

Program Manager

The AFOSR Program Manager currently assigned to the award

Tatjana CURCIC

Reporting Period Start Date

06/01/2012

Reporting Period End Date

11/30/2015

Abstract

The goal of the project "Modular Paradigm for Scalable Quantum Information" was to address some of the challenges facing the field of quantum information science (QIS). The requirements to reliably control a scalable quantum system while staving off decoherence pose a contradiction, as fast control implies a strong coupling to a controlling (external) system, but this entails an undesired interaction with the environment, leading to decoherence. We thus studied a new paradigm for QIS, given by smaller building blocks (composed of a quantum register and an actuator) that are connected by spin wires.

The project had activities along these two lines of research.

On one side, we studied the working principles of the actuator/register model, in particular its control and the indirect control of the quantum register.

We developed a comprehensive theory of time-optimal control of the quantum register, finding a minimal set of parameters that need to be optimized to obtain the time-optimal control sequence for any desired quantum gate. This enables us to devise an efficient numerical method to find the time-optimal sequence and in turn to investigate its performance on a realistic system.

In addition, we developed experimental control of an exemplary actuator/register system, the nitrogen-

vacancy (NV) electronic spin center in diamond and its associated nitrogen nuclear spin.

We used the control to characterize the Hamiltonian of the system and to achieve enhanced control speed, exploiting the presence of the quantum actuator. In addition, we showed how to use a quantum controller to perform quantum feedback, to protect the qubit systems from decoherence.

The main results of this first task are:

- We found the shape of the time-optimal control strategy to engineer desired qubit gates via the actuator control. Using algebraic methods we were able to find the time-optimal control solutions for the most general $SU(2)$ synthesis problem.

- We developed an efficient numerical method to find the time-optimal control sequence and applied it to find gates for the coupled NV-nuclear spin system.

- We exploited an hybrid control strategy, combining classical and quantum controllers, to achieve faster control of a nuclear spin qubit.

- We exploited a long-lived spin qubit as a controller to implement quantum feedback to preserve the coherence of the NV electronic spin

Our activities demonstrated that quantum controllers can provide powerful advantages over classical controllers, achieving faster and more robust control and make new tasks, such as feedback control, possible.

For the second activity of the program we explored quantum information transfer using quantum spin wires, which transport information via the free evolution under their mutual interaction.

We combined a theoretical study of the conditions for perfect quantum state transfer with an experimental investigation the role of decoherence and disorder in the transport process, using an experimental implementation with nuclear magnetic resonance techniques applied to apatite crystals.

Results we achieved pertinent to this second task include:

- We performed the first experimental implementation of quantum information transfer in mixed-state spin chains.

- We devised protocols for Hamiltonian engineering that can lead to perfect quantum information transfer even in the absence of single-spin addressability. These techniques can be more generally used for quantum simulations in a variety of quantum systems.

- We found that the restriction of the spin system to one-dimensional geometries yields a complex, non-Markovian decoherent dynamics. However, it also makes the coherence times longer than in 3D systems, thus pointing to advantages to be found in particular geometries for larger quantum information architectures.

- We studied the polarization transfer from NV centers in diamond (that can be polarized optically) to dark spins associated with single Nitrogen defects (P1 centers) in diamond. We positively assessed the potential of this system for a scalable quantum information architecture.

Our results provide new powerful tools for achieving robust quantum wires and strategies for counteracting the effects of noise and disorder. At the same time, we devised novel techniques that have broader impacts on quantum simulations, from Hamiltonian engineering to novel ways of engineering the bath.

Distribution Statement

This is block 12 on the SF298 form.

Distribution A - Approved for Public Release

Explanation for Distribution Statement

If this is not approved for public release, please provide a short explanation. E.g., contains proprietary information.

SF298 Form

Please attach your SF298 form. A blank SF298 can be found [here](#). Please do not password protect or secure the PDF. The maximum file size for an SF298 is 50MB.

[AFD-070820-035 final.pdf](#)

Upload the Report Document. File must be a PDF. Please do not password protect or secure the PDF. The maximum file size for the Report Document is 50MB.

[YIP_report15.pdf](#)

Upload a Report Document, if any. The maximum file size for the Report Document is 50MB.

Archival Publications (published) during reporting period:

A. Ajoy and P. Cappellaro, "Mixed-state quantum transport in correlated spin networks"
Phys. Rev. A 85, 042305 (2012)

G. Kaur and P. Cappellaro, "Initialization and readout of spin chains for quantum information transport"
New J. Phys. 14, 083005 (2012)

A. Ajoy and P. Cappellaro, "Perfect quantum transport in arbitrary spin networks"
Phys. Rev. B 87, 064303 (2013)

A. Ajoy and P. Cappellaro, "Quantum simulation via filtered Hamiltonian engineering: application to perfect quantum transport in spin networks"
Phys. Rev. Lett. 110, 220503 (2013)

G. Kaur, A. Ajoy and P. Cappellaro, "Decay of spin coherences in one-dimensional spin systems"
New J. Phys. 15, 093035 (2013)

C. Belthangady, N. Bar-Gill, L. M. Pham, K. Arai, D. Le Sage, P. Cappellaro and R. L. Walsworth
"Dressed-State Resonant Coupling between Bright and Dark Spins in Diamond"
Phys. Rev. Lett. 110, 157601 (2013)

P. Cappellaro
"Implementation of State Transfer Hamiltonians in Spin Chains with Magnetic Resonance Techniques"
In Quantum State Transfer and Network Engineering , 183-222 (2014)

C. Aiello, M. Allegra, B. Hemmerling, X. Wan and P. Cappellaro
"Algebraic synthesis of time-optimal unitaries in SU(2) with alternating controls"
Quantum Information Processing 14, 3233 (2015)

C. D. Aiello and P. Cappellaro
"Time-optimal control by a quantum actuator"
Phys. Rev. A 91, 042340 (2015)

M. Chen, M. Hirose and P. Cappellaro
"Measurement of transverse hyperfine interaction by forbidden transitions"
Phys. Rev. B 92, 020101 (2015)

M. Hirose and P. Cappellaro
"Time-optimal control with finite bandwidth"
Arxiv:1510.06801(2015)

M. Hirose and P. Cappellaro "Coherent feedback control of a single qubit in diamond", to appear in Nature, (2016).

Changes in research objectives (if any):

Change in AFOSR Program Manager, if any:

Extensions granted or milestones slipped, if any:

AFOSR LRIR Number

LRIR Title

Reporting Period

Laboratory Task Manager

Program Officer

Research Objectives

Technical Summary

Funding Summary by Cost Category (by FY, \$K)

	Starting FY	FY+1	FY+2
Salary			
Equipment/Facilities			
Supplies			
Total			

Report Document

Report Document - Text Analysis

Report Document - Text Analysis

Appendix Documents

2. Thank You

E-mail user

Mar 01, 2016 12:45:12 Success: Email Sent to: pcappell@mit.edu